

# Multiferroicity in plastically deformed SrTiO<sub>3</sub>

Received: 20 September 2023

Accepted: 14 August 2024

Published online: 28 August 2024

Check for updates

Xi Wang <sup>1,2,10</sup>, Anirban Kundu<sup>3,10</sup>, Bochao Xu <sup>4,10</sup>, Sajna Hameed<sup>5,9</sup>, Nadav Rothem <sup>1,2</sup>, Shai Rabkin <sup>1,2</sup>, Luka Rogic<sup>6</sup>, Liam Thompson<sup>5</sup>, Alexander McLeod <sup>5</sup>, Martin Greven <sup>5</sup>, Damjan Pelc <sup>6</sup>, Ilya Sochnikov <sup>4,7,8</sup>, Beena Kalisky <sup>1,2</sup> ✉ & Avraham Klein <sup>3</sup> ✉

Quantum materials have a fascinating tendency to manifest novel and unexpected electronic states upon proper manipulation. Ideally, such manipulation should induce strong and irreversible changes and lead to new relevant length scales. Plastic deformation introduces large numbers of dislocations into a material, which can organize into extended structures and give rise to qualitatively new physics as a result of the huge localized strains. However, this approach is largely unexplored in the context of quantum materials, which are traditionally grown to be as pristine and clean as possible. Here we show that plastic deformation induces robust magnetism in the quantum paraelectric SrTiO<sub>3</sub>, a property that is completely absent in the pristine material. We combine scanning magnetic measurements and near-field optical microscopy to find that the magnetic order is localized along dislocation walls and coexists with ferroelectric order along the walls. The magnetic signals can be switched on and off via external stress and altered by external electric fields, which demonstrates that plastically deformed SrTiO<sub>3</sub> is a quantum multiferroic. These results establish plastic deformation as a versatile knob for the manipulation of the electronic properties of quantum materials.

One of the most sought-after properties of quantum materials is the manifestation of multiple order parameters, either in coexistence or by “switching” between states via external stimuli. Since charge, spin, superconducting, topological and other orders are crucial for quantum technologies, multi-order systems are expected to be of significant value to future applications. One pathway to creating multi-order systems is to take a compound with known properties and introduce additional ordered states via doping or interfacing with a different compound<sup>1–3</sup>. An alternative route that has been receiving much recent attention is strain engineering. This approach has been used, or proposed as an avenue to induce magnetism, ferroelectricity and other ordered states, to enhance superconductivity, and to create novel excitations<sup>4–11</sup>. However, this approach typically involves

relatively small elastic strains and is not a permanent modification – once the stress is removed, the new properties vanish. In contrast, plastic deformation leads to large local strains and induces permanent modifications. This approach is widely used in materials engineering<sup>12–15</sup>, but has received comparatively little attention in the quantum materials community. Conventional wisdom holds that quantum materials, especially metallic and superconducting systems, should be as clean and pristine as possible, while plastic deformation induces many defects and strong geometric deformations. However, a recent study found that, in stark contrast to this preconception, plastic engineering can induce a permanent enhancement of superconductivity and ferroelectricity in the unconventional superconductor SrTiO<sub>3</sub> (STO) as a result of self-organized, periodic

<sup>1</sup>Department of Physics, Bar-Ilan University, Ramat Gan, Israel. <sup>2</sup>Institute of Nanotechnology & Advanced Materials, Bar-Ilan University, Ramat Gan, Israel. <sup>3</sup>Department of Physics, Ariel University, Ariel, Israel. <sup>4</sup>Department of Physics, University of Connecticut, Storrs, CT, USA. <sup>5</sup>School of Physics and Astronomy, University of Minnesota, Minneapolis, MN, USA. <sup>6</sup>Department of Physics, Faculty of Science, University of Zagreb, Zagreb, Croatia. <sup>7</sup>Institute of Materials Science, University of Connecticut, Storrs, CT, USA. <sup>8</sup>Materials Science and Engineering Department, University of Connecticut, Storrs, CT, USA. <sup>9</sup>Present address: Max Planck Institute for Solid State Research, Stuttgart, Germany. <sup>10</sup>These authors contributed equally: Xi Wang, Anirban Kundu, Bochao Xu. ✉ e-mail: [beena@biu.ac.il](mailto:beena@biu.ac.il); [avrahamk@ariel.ac.il](mailto:avrahamk@ariel.ac.il)

dislocation structures<sup>16</sup>. This intriguing discovery suggests that plastic engineering of quantum materials ought to be far more thoroughly explored<sup>17,18</sup>.

Here, we show that plastic deformation generates intrinsic magnetism in STO that is completely absent in pristine samples. The magnetic order is strongly coupled to ferroelectric order, and both are induced by nanoscale dislocation structures, in both insulating and metallic (superconducting) samples. The successful conversion of a ferroelectric and superconducting compound into a low-temperature multiferroic system establishes plastic deformation as a powerful tool for quantum materials design and study.

STO is a well-known unconventional superconductor and an incipient ferroelectric (FE)<sup>19</sup> that maintains its inversion-breaking properties upon doping with charge carriers<sup>20–24</sup>. Pristine STO is typically considered nonmagnetic and exhibits a weak bulk diamagnetic response. However, there have been persistent hints of emergent magnetism in bulk samples and various STO-based interfaces<sup>20,25–37</sup>, which has triggered an ongoing debate on the subject<sup>35,38–41</sup>. There has also been a significant effort to study the relationship between superconductivity and magnetism in STO interfaces<sup>27,28,42,43</sup>. In addition, STO crystals are surprisingly ductile even at ambient temperature, with plastic deformation levels up to ~10% achieved in both insulating and metallic samples<sup>16,44</sup>. Plastic deformation leads to the formation of self-organized, quasi-two-dimensional dislocation structures – dislocation walls – surrounded by a field of high strain. The local atomic displacements in these dislocation walls are comparable to the unit cell dimensions<sup>16,45</sup>, and the dislocations themselves are organized in chains with an inter-dislocation spacing on the order of nanometers, elegantly bridging the gap from the atomic to the macroscopic scale. This material is therefore a prime candidate for the exploration of emergent properties through plastic strain engineering.

In order to study the effect of plastic deformation on magnetism, we perform magnetic measurements on the micron scale. We find a robust stripe-like magnetic landscape in both insulating and conducting STO, and attribute this pattern to the localization of magnetism at the dislocation walls that run perpendicular to the deformation axis. Furthermore, we perform near-field infrared imaging of the stripe-like features with submicron spatial resolution, and confirm their origin to be nanoscale dislocation structures. Our local information on the dislocation structure complements previous Raman scattering measurements of ferroelectricity near the dislocations<sup>16</sup>,

and demonstrates that both the ferroelectric and magnetic orders are intrinsic and arise from magneto- and polar-elastic interactions. Even more remarkably, by applying voltage to a gated sample, we show that the magnetic signal responds to an externally applied *electric* field. Our data and theoretical analysis show that the two orders are strongly correlated, and we thereby establish that plastically deformed STO is a quantum multiferroic. Our work demonstrates the potential power of plastic deformation engineering in quantum materials: we generate magnetism which is orders of magnitude stronger than other strain-induced effects, e.g., from domain walls, without introducing external charge dopants. Furthermore, ferroelectricity and magnetism are induced by the same microstructures (the dislocation walls), which render them strongly coupled and allow us to study them in tandem.

## Results

### Stripe magnetism in plastically deformed STO

In this study, we examine three types of plastically deformed STO: metallic samples doped with niobium or oxygen vacancies, and undoped, insulating samples. In order to map the normal-state local magnetic landscape of deformed STO we employ scanning superconducting quantum interference device (SQUID) microscopy between 5 K and 16 K, a temperature range in which quantum FE fluctuations are expected to be strong<sup>33,46</sup>. The sketch in Fig. 1a illustrates our measurement setup (see section “Methods” for further details). The scanning SQUID contains a micron-sized pick-up loop on a tip and a coil to generate external magnetic fields. This enables the detection of both spontaneous and field-generated magnetism with a high spatial resolution. The tip-to-sample distance can be varied, including to a zero-distance configuration where the tip is in mechanical contact with the sample. This approach allows us to investigate and characterize the magnetic properties of plastically deformed STO at the micron scale.

We report two main findings. Our first finding is the detection of robust stripe-like signatures of magnetism, but *only* when the tip is in contact with the sample. This is seen in Fig. 1d–g, which show SQUID images of both magnetic order and paramagnetic susceptibility as a function of two-dimensional space when scanning in contact, with similar results for both observables. The stripe-like modulation is also found in the stress-sensing capacitance channel, as shown in Fig. 1c. The orientation of stripes in the SQUID images is consistent with the direction of the dislocation walls formed during deformation (see

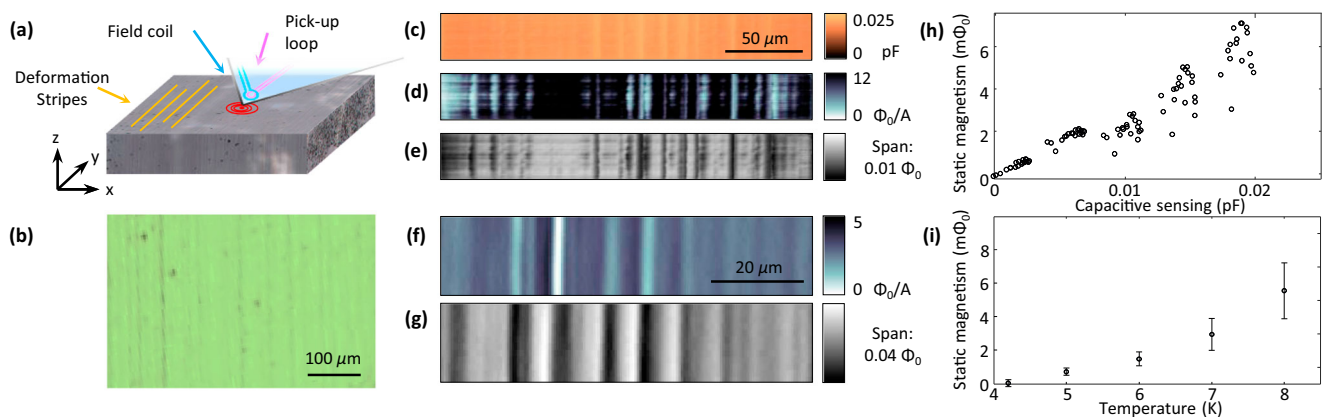


**Fig. 1 | Scanning SQUID measurement and stripy magnetic order in plastically deformed SrTiO<sub>3</sub> observed by scanning in contact with the surface of the sample.** **a** Illustration of scanning SQUID measurement in contact mode (Note that our axes choice is different from that in ref. 16, where the deformation axis was [010] or  $\bar{y}$ ). **b** Optical images of the sample. The deformation stripes are visible on the surface. **c–e** Scanning SQUID images of capacitive surface sensing, susceptibility, spontaneous magnetism, respectively, in an undoped sample (sample 4).

The magnetic stripe direction coincides with that of the deformed stripes shown in (b). **f, g** Susceptibility and spontaneous magnetism, respectively, in a conducting sample (Nb doped, sample 2). **h** Stress dependence of the magnetism exhibits linear behavior (see also Fig. 2a). The capacitive reading is proportional to the force exerted on the sample, see section “Methods”. **i** The strength of the magnetism (see also 2b) increases with increasing temperature. Both the stress and the temperature dependence are explained by the phenomenological model we suggest.

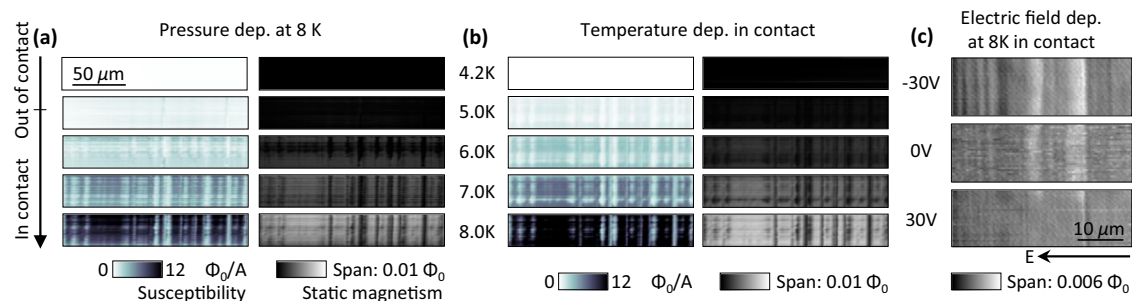


**Fig. 2 | Stress, temperature, and electric field dependence of magnetic signal in undoped, plastically deformed SrTiO<sub>3</sub>.** **a** Stress dependence of magnetic stripes in susceptibility and magnetometry at 8 K in undoped sample 4. Before contact (lift-off height of 0.6  $\mu\text{m}$ ) with the surface by the SQUID tip, we observe only background noise. The magnetic response increases with the applied force. **b** Temperature dependence of magnetic stripes by scanning in contact, in undoped sample 4. The applied force is estimated to be 0.1–1  $\mu\text{N}$  (Note: this range is rather

uncertain because of the nonuniform surface). The magnetic response increases with the temperature. (Further temperature ranges can be found in the SI Figs. S2 and S3). **c** Electric field dependence of magnetic stripes in the gated sample 5. The arrow indicates that the electric field is applied in-plane, perpendicular to the direction of the deformation stripes. The details of the gate dependence require further investigation. See SI Fig. S1.

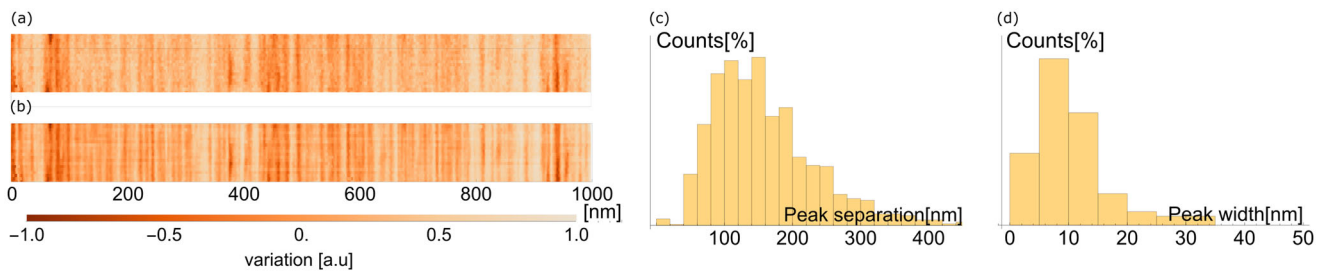


**Fig. 3 | Nano-infrared imaging of optical phonon contrasts at an energy of 100 meV along the surface of an undoped 2.4% deformed crystal.** Variations of the absorption coefficient amplitude **(a)** and phase **(b)** in a 1000 nm  $\times$  100 nm strip (see section “Methods” for details). Striped contrast made clearly visible by the Grüneisen effect show that stresses and strains are localized to dislocation walls. The inferred strain variations (averaged over the experimental spot size and penetration depth; see SI) are of order 0.1%, implying localized strains of order unity near

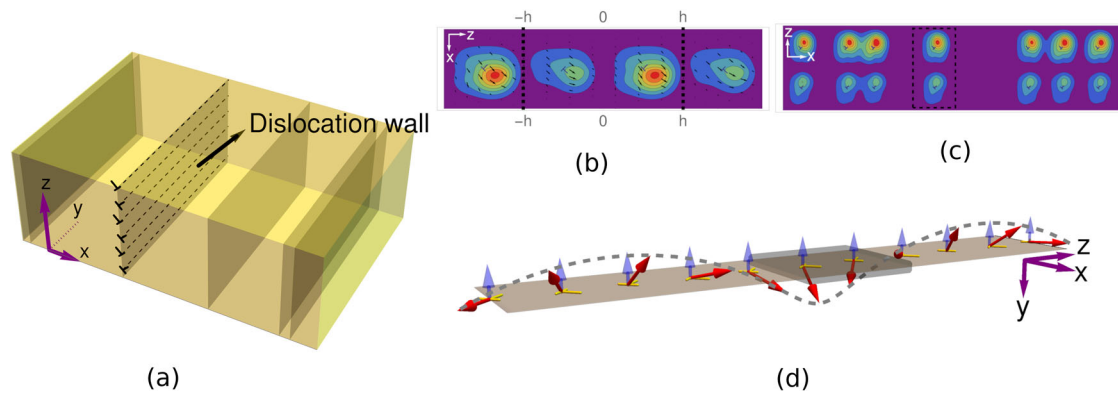
the dislocations (see section “Methods”). **c** A histogram of the nearest-neighbor separation of the absorption amplitude peaks, revealing that the typical dislocation separation is approximately 100 nm. The data for the phase is qualitatively the same (see SI). **d** A histogram of the typical width of a peak, showing that the peak width is approximately 10 nm, which is comparable with the resolution of our experiment, confirming that strain is highly localized to the stripes.

Fig. 1b and discussion below). Within instrumental resolution, no magnetic signal is found in non-contact mode (Fig. 2a). The magnetic signal increases linearly with applied stress (Fig. 2a), accompanied by enhanced contrast in the magnetic stripes (Fig. 2a), before saturating at an applied force of approximately 1  $\mu\text{N}$ <sup>33</sup>. This signal is strongly modified by applying an electric field perpendicular to the stripes (Fig. 2c and SI Fig. S1). The dependence of the signal on stress remains even in the presence of electric field. As we discuss in the next section, the puzzling stress dependence is mostly likely due to an in-plane ferromagnetic order that is canted out of the plane by the external contact.

Our second main finding is that the in-contact magnetic signal strength increases with temperature up to at least 16 K (Figs. 1i, 2b and SI Figs. S2, S3). This is in contrast to the conventional situation where magnetic order decreases with increasing temperature. We were unable to perform measurements above 16 K, since at higher temperatures the SQUID loop cannot be kept superconducting while the chip is in physical contact with the sample. The observed behavior is consistent across all our measured samples - both insulating and (super)conducting. We do note that, in the Nb-doped sample 1, we found magnetism only in a small region on the crystal surface (see SI Fig. S4), and some signatures of deformation stripes in the superconducting phase (SI Fig. S5, measurements performed at  $T \approx 0.02\text{K}$ ). This variation of the spatial distribution may be related to inhomogeneity of the surface profile.

The two principal observations, the stress- and temperature-dependent magnetic signals, are highly robust, since the same results are obtained by two independent scanning SQUID groups, in distinct samples from different sample sources. The magnetic signal is roughly two orders of magnitude stronger than in previous measurements of in-contact magnetic signal in LaAlO<sub>3</sub>/STO interfaces and pristine STO domain walls<sup>33</sup>. We note that an unconventional signal increase with temperature was found in those experiments as well. If we assume that the observed magnetic signal stems from an effective surface magnetization,  $m_s$ , we may estimate  $m_s \sim 1\mu_B/a_0^2$ , where  $\mu_B$  is the Bohr magneton and  $a_0 \approx 4 \text{ \AA}$  is the STO lattice constant (see section “Methods”). This conservative estimate is not based on any specific theoretical microscopic consideration. We do not have a quantitative estimate of the magneto-electric coupling in our samples, but, as Fig. 2c shows, the coupling is clearly strong enough to qualitatively modify the magnetic signal.

In order to gain further insight into the origin of the stripe-patterned magnetization signals, we perform nanometer-resolved scanning near-field optical microscopy (SNOM) measurements<sup>47</sup> on our deformed samples. Figure 3 shows the results of near-field optical microscopy on an undoped deformed sample (sample 6, see section “Methods”). This SNOM-based nano-infrared (nano-IR) imaging approach directly probes the optical properties of surfaces with a  $\sim 10 \text{ nm}$  spatial resolution<sup>48</sup>. Our nano-IR measurements employ illumination from an ultrafast laser source tuned to the energy of the



**Fig. 4 | Depiction of the theoretically expected magnetic configuration from several different perspectives.** **a** Sketch of the randomly distributed dislocation walls and the Burgers vector orientations (Note that our axes choice is different from that in ref. 16, where the deformation axis was [010] or  $\hat{y}$ ). **b** Magnetic order along a dislocation wall. The dislocation wall consists of a repeating unit cell (dashed lines) of two dislocations (purple Burgers vectors), and elastomagnetic coupling induces a nonzero magnetic moment  $\mathbf{m}$  whose magnitude is strongly localized in “puddles” near the dislocations (heatmap, arbitrary units). The planar projection ( $m_x, m_z$ ) of  $\mathbf{m}$  (black arrows) is shown in an “antiferromagnetic”

configuration of  $m_z$ , and “ferromagnetic” configuration of  $m_x$ . This order is nearly degenerate with a fully ferromagnetic one. **c** Magnetic order in a region occupied by a random series of dislocation walls. The dashed region marks the area in the unit cell of **(b)**. **d** Illustration of a possible spin-spiral structure of the coarse-grained spin-chain model of the dislocation wall. Blue arrows denote the constant background FE field direction, and red arrows the rotating magnetic moments. Only  $m_x$  remains ferromagnetic, which explains why there is no out-of-contact magnetic signal.

highest zone-center optical phonon of STO<sup>49</sup> which is focused to the sharp tip of a metallized probe (curvature radius  $\approx 20$  nm). When brought within nanometers of the sample surface, the probe polarization, in both phase and amplitude, is modulated through near-field interactions with its dielectric environment (see section “Methods”). This produces a spatially resolved infrared “near-field” signal that quantifies the optical response of the surface, and can be directly correlated with local strain variations (Fig. 3a, b). Such variations were undetectable in undeformed STO samples. By associating observed nano-infrared contrasts with strain variations<sup>50</sup>, and see section “Methods”), we conclude that strains in our deformed STO orient as sharp stripes (Fig. 3a, b), with a typical inter-stripe distance of 50–100 nm (Fig. 3c) and a characteristic width which appears to be only limited by the spatial resolution of the optical nano-probe ( $\sim 10$  to 20 nm, Fig. 3d). Such straight lines of strong, nanoscale localized strain fluctuations indicate the existence of a dense distribution of dislocation walls running parallel to each other, perpendicular to the surface and the deformation axis (see Fig. 4a). Our analysis shows that strain variations, averaged over the resolution, are on the order of 0.1%. This result is consistent with the existence of dislocation-induced strains of order unity (see section “Methods”), as such strain fields are multipolar and periodic. Our findings are also quantitatively consistent with previous bulk X-ray and neutron diffuse scattering results<sup>16</sup>, which indicated the existence of dislocation walls running perpendicular to the deformation axis. The scattering measurements are of course unable to directly detect such walls in real space, but analysis of interference patterns can be used to determine their structure. The walls were found to consist of pairs of dislocations with Burgers vectors along the unit cell face diagonal, (e.g. [101], [10-1]), with an inter-dislocation distance of approximately  $h = 14a_0$  (Note that our axes choice is different from that in ref. 16, where the deformation axis was [010] or  $\hat{y}$ ). The unit cell of a wall therefore has a length of  $2h$ .

As we describe below (see next section), such dislocation walls have strain profiles that decay on a scale of  $2h \sim 10$  nm. In addition, it is well known that strains as small as  $\sim 0.1\%$  are enough to drive STO into a FE state (ref. 5 and SI), and since dislocations induce strains of order unity, our strain measurements imply that long-range polar order is present in sheets localized near the dislocation walls. Indeed, previous polarized Raman scattering experiments (see ref. 16 and SI Fig. S10) have established that deformed STO hosts coexisting polar order and

soft polar fluctuations consistent with the quantum paraelectric state of bulk STO. Our scanning optical measurements, together with the previously reported bulk measurements of diffuse neutron, X-ray, and Raman scattering, thus confirm the picture of parallel dislocation walls running perpendicular to the surface and hosting magnetic signals, with robust local FE order at the walls.

#### Coupling of dislocations, magnetism, and ferroelectricity

The dramatic difference between plastically deformed and pristine samples indicates that lattice degrees of freedom play a crucial role. It is unlikely that the magnetic signal is induced by the tip contact itself, as previous in-contact measurements on undeformed STO and LaAlO<sub>3</sub>/STO and  $\gamma$ -Al<sub>2</sub>O<sub>3</sub>/STO interfaces found magnetic signals orders of magnitude smaller<sup>33</sup>. The SQUID signals therefore must arise from deformation-induced regions of both static magnetic order and paramagnetism in close proximity to each other. This is consistent with magnetism localized near the dislocation walls, surrounded by paramagnetic regions. Furthermore, the magnetic moments must be ordered so that they can only be detected when stress is applied by the tip. This indicates the magnetic order is either homogeneous, i.e. ferromagnetic, but in the plane parallel to the surface ( $xy$  plane in Fig. 1a), or an inhomogeneous, e.g., spiral, order. In both these cases the out-of-plane magnetic field picked up by the SQUID would average to zero, and would only be detected if the tip stress rotated the magnetic order to induce an out-of-plane ferromagnetic component. In addition, it is unlikely that the magnetism is triggered by local charge doping in the walls, as the magnetic signal is qualitatively the same for insulating and conducting samples; as noted, the latter are probably superconducting along the same dislocation walls. Finally, the magnetic order must have an effective coupling to external electric fields. We now show that our results are naturally explained by coincident magnetic and FE order, induced directly by the strong deformation of the lattice at the dislocations and the large associated strains, and mutually interacting.

To this end, we construct an effective low-energy model that describes the interplay between strain, magnetism and FE order. For simplicity, we assume that the walls are randomly distributed perpendicular to the deformation, which we choose as the  $\hat{x}$  axis – see Fig. 4a for a schematic (Note that our axes choice is different from that in ref. 16, where the deformation axis was [010] or  $\hat{y}$ ). Since the



dislocation spacing  $h \gg a_0$ , the physics should be at least qualitatively captured by a continuum theory, and we therefore construct a Ginzburg-Landau free energy for the coupled magnetic moment  $\mathbf{m}$ , strain  $\epsilon_{ij}$ , and FE order  $\mathbf{u}$ . In STO,  $\mathbf{u}$  in both insulating and conducting samples represents a zone-center polar phonon, whose condensation mediates the breaking of inversion symmetry. Due to Coulomb forces, only the transverse components of  $\mathbf{u}$  are relevant at low temperatures, so we assume  $\nabla \cdot \mathbf{u} \approx 0$ . We neglect additional degrees of freedom, e.g.,  $\mathbf{u}$ 's corresponding longitudinal mode, or additional zone-boundary phonons that can be expected to only quantitatively change the results. We assume that the dislocations in each wall (see Fig. 4a) run parallel to the scanning surface, since it can be checked that the magnetic signal from dislocations running parallel to the surface will be stronger than those from dislocations terminating at the surface. Thus, the dislocations have an axis that runs along  $\hat{y}$ , and so our fields are (except for negligible boundary effects) independent of  $y$ , e.g.  $\mathbf{m} = \mathbf{m}(x, z)$ .

We summarize here the results of our analysis, details of which are provided in the Methods section. Both  $\mathbf{u}$  and  $\mathbf{m}$  orders are described by simple quartic free energies, coupled to strain,

$$F_n = \int dx dz \left[ \frac{a_n}{2} |\boldsymbol{\eta}|^2 + \frac{b_n}{4} \sum_j \eta_j^4 + \boldsymbol{\eta} \cdot (\hat{\Lambda}_n \hat{\epsilon}) \cdot \boldsymbol{\eta} \right], \quad (1)$$

where  $\boldsymbol{\eta} = m, u$  and  $\hat{\Lambda}_n \hat{\epsilon} \equiv \lambda_n^{ijkl} \epsilon_{kl}$  is a strain-coupling tensor whose elements are dictated by the undeformed lattice symmetries. The strong strains near dislocations drive both magnetic and FE order, since  $\epsilon_{ij}$  couples to quadratic terms of both  $\mathbf{m}$  and  $\mathbf{u}$  in the free energy, and the dipolar strain fields of a dislocation ensure that some regions around the dislocation are always favorable to order. By construction, the FE order is “soft”, with  $a_u \ll a_m$ , consistent with the proximity of clean STO to a FE state, and has strong elastic coupling  $|a_u| \ll |\lambda_u|^{51,52}$ . Hence, the region of induced  $\mathbf{u}$  order is far more extensive than the ordered  $\mathbf{m}$  regions. This gives rise to localized “puddles” of magnetism around each dislocation, and to quasi-long-range FE order along the walls (see Fig. 4b, c for a depiction of the calculated magnetic puddles). Interestingly, interference effects, the complex unit cell, and the discrete symmetry of even the simplest lattice (we take a cubic lattice), imply that the strain fields are sufficiently complicated to induce nonzero and inhomogeneous values of all three components of magnetic field around a given dislocation. In particular,  $m_z(x, z) \neq 0$ , in contradiction to the absence of a “no-contact” signal (Fig. 1h). Furthermore, the temperature dependence of  $\mathbf{m}$  (Fig. 1i) is also inconsistent with pure strain-induced magnetism, which should lead to Curie-like or, even more probably, a constant- $T$  dependence. We must therefore take a step further and investigate the long-range effective interactions among magnetic puddles.

We find that, due to a single remaining intra-unit-cell  $z$ -axis inversion symmetry and the relatively large distance between dislocations, different magnetic puddles are approximately magnetically uncoupled, so that a dislocation wall can be thought of as a series of noninteracting spins (one spin per puddle). Thus, the long-range FE order is a natural candidate to mediate long-range spin-spin interactions. As opposed to the magnetic order, the FE polarization is strongly constrained by its transverse nature. The complicated strain fields always induce longitudinal deformations, except for the case where  $\mathbf{u} = u_y(x, z)\hat{y}$ , i.e., when the FE order is parallel to the dislocations themselves. Symmetry constraints imply two allowed couplings: biquadratic ( $-\mathbf{m}^2 \mathbf{u}^2$ ) and magneto-flexupolar, Dzyaloshinskii-Moriya-like ( $-\mathbf{u} \mathbf{m} \nabla \mathbf{m}$ ) coupling. The biquadratic term readily accounts for the magnetic  $T$  dependence, if the coupling is repulsive. The second term, once the directional constraint of  $\mathbf{u}$  is accounted for, naturally induces a spiral or helical order for  $\mathbf{m}$  in the  $yz$  plane (see Fig. 4d). Such a configuration shows no out-of-plane moment. In the presence of a force provided by the tip, a longitudinal FE component is again

introduced, causing  $\mathbf{u}$  polarization to rotate and drag the  $\mathbf{m}$  moments with it. This induces an out-of-plane ferromagnetic component and a signal in contact.

We now briefly discuss the electric field dependence. First, the strong response of the stripes themselves (see Fig. 2c) indicates that, as discussed above, the FE and magnetic order coexist on the dislocation walls. Given the huge dielectric susceptibility ( $\sim 10^4$ ) of pristine STO, our applied voltages of order  $\sim 10$  V can only yield energy shifts of order of meV in the bulk. This is comparable to the transverse phonon energy and is well below the longitudinal mode energy scale. Hence we may expect the FE order to remain approximately transverse, and therefore correlated with the dislocation lines. Applying a perpendicular electric field likely creates angular shifts due to the large spatial variations of strains, which can disorder the magnetic in-plane order and wash out the signal. A detailed calculation of the magnetoelectric susceptibility would require a modeling of the coupled dislocation, FE and magnetic orders under the external fields, which is beyond the scope of the present work.

## Discussion

The observed magnetism is a result of plastic strain engineering. Our analysis reveals that the magnetism is induced at the self-organized dislocation walls. In terms of magnitude, the measured signals of  $\sim 1 \mu_B$  per surface unit cell are on the order of what has been reported for carrier-doped STO. We, however, find similar magnitudes for undoped samples as well, indicating that the source of the magnetism is not doped carriers but rather strain. We note that STO shows a structural transition to a tetragonal phase at 105 K, leading to tetragonal domains at low temperatures, which could generate magnetism as well. However, although the domain walls probably do participate in the induced magnetism, previous measurements of magnetic signals at the walls are two orders of magnitude weaker than what we observe<sup>33</sup>. This indicates that plastic deformation induces far larger localized strains.

The observed temperature dependence deserves some discussion, since it is opposite to the Curie-type decrease with temperature typical of paramagnetic and ferromagnetic materials. Doped STO, where paramagnetism is expected, shows low- $T$  Curie-type behavior<sup>35</sup>, although there are also conflicting reports of anomalous magnetism under various conditions, which tends to be much weaker than in our work. The magnetic signals we observe are robust even in undoped samples, making doping effects less likely. As discussed above, our phenomenological model naturally attributes the  $T$  dependence to the competition between the induced magnetism and the dominant FE phase near the dislocation walls. This contradicts conventional wisdom that magnetism (especially spiral magnetism) should be induced by inversion-symmetry breaking<sup>39</sup>. Below we discuss a few possible microscopic effects that might be related to the magnetism reported here.

Our results raise two interrelated questions regarding the microscopics of the magnetism: what is the source of the paramagnetism near the dislocations, and what determines the strength of the magnetoelastic coupling that induces static order. Previous studies have shown that STO dislocation strain can change the Ti valence by as much as  $\sim 1/2$ <sup>53</sup>, which raises the possibility that  $\text{Ti}^{3+}$  states near the dislocations give rise to paramagnetism, analogous to the magnetic properties found in rare-earth titanates such as  $(Y, \text{La})\text{TiO}_3$ <sup>54</sup>. Such effects could be the cause of both the paramagnetism and the magnetoelastic properties. Another idea for paramagnetism in STO is that coherent motion of polar moments induces paramagnetic fluctuations. These can arise via Faraday's law, either from the motion of polar domains and associated charged defects, or from virtual fluctuations near the FE quantum critical point<sup>34,55,56</sup>. This mechanism also naturally accounts for the repulsive biquadratic term and the temperature dependence of the magnetism, since the effect is suppressed in the ordered state. However, the magnitude of the magnetic signals that we

observe is considerably larger than predicted from coherent virtual motion. It should be possible to distinguish between these two effects at high temperatures in future experiments, where coherent FE motion would be suppressed, but the Ti-ion effects would remain.

The scanning SQUID technique is particularly suitable for the detection of deformation-induced local magnetism, due to its high spatial resolution and magnetic sensitivity, and the ability to apply force with the tip. Unfortunately, its stringent temperature limitations preclude any investigation of the magnetism at higher temperatures. The use of complementary techniques would therefore be highly desirable, although the conjectured spiral order and small volume fraction (at most a few percent, see Methods) present unique challenges to bulk probes such as neutron diffraction, magnetometry, muon spin resonance and NMR. We expect that any complementary local measurement with an equivalent sensitivity, such as MOKE, MFM, or NV-SPM in the presence of external stress, would yield similar results. Highly sensitive resonant x-ray techniques such as nanobeam magnetic circular dichroism (XMCD) might be the most suitable to shed further light on this effect, including the intriguing possibility of near-ambient temperature magnetism in deformed STO.

Conceptually, the most important result of our work is that the large local strains accompanying dislocation structures can induce and enhance quantum materials properties that are otherwise essentially unavailable. Furthermore, the new properties appear on the nanoscale, opening an avenue to intertwine the new properties with the old bulk. Using STO as a model system, we demonstrate the tremendous potential of plastic deformation as a quantum materials engineering tool. Some of the key characteristics of this approach are its simplicity, the ability to use macroscopic bulk samples, and a vast available parameter space – deformation temperature, stress rate and direction can all be varied in a wide range. We anticipate that this approach will enable the creation of self-organized dislocation networks in many other quantum materials of interest, and that other, more tailored approaches could lead to similar results, with further enhanced controllability and the possibility to create micron-scale devices. Some avenues worthwhile of further investigation are fusing of surfaces to create low-angle grain boundaries, engineering of large epitaxial lattice mismatch, and nanoindentation, all of which are routinely used in materials science to engineer and manipulate dislocation structures. Another avenue is combining plastic deformation with other experimental knobs, e.g., oxygen-vacancy doping, which has been suggested as a source of magnetism in STO based heterostructures. Overall, we believe that the present work points the way to an exciting possibility of a large-scale quantum-materials engineering effort.

## Methods

### Samples

We examined four types of plastically deformed SrTiO<sub>3</sub> crystals: (i) doped SrTi<sub>1-x</sub>Nb<sub>x</sub>O<sub>3</sub> ( $x = 0.002$ , SI Fig. S4 and S5, named sample 1), previously reported to exhibit enhanced superconductivity at low temperatures, prepared by the Minnesota and Zagreb groups from commercial crystals (MTI Corp.)<sup>16</sup>, and SrTi<sub>1-x</sub>Nb<sub>x</sub>O<sub>3</sub> ( $x = 0.004$ , Fig. 1 and SI Fig. S2, sample 2), sourced from Furuuchi Chemical<sup>9</sup>, plastically deformed by the Connecticut group; (ii) a conducting oxygen-vacancy-doped sample (carrier density  $\sim 4 \times 10^{17} \text{ cm}^{-3}$ , Fig. S3, sample 3), (iii) an undoped, insulating sample for detailed magnetic measurements (Figs. 1 and 2a, b, sample 4), and another similar sample for the nano-optics, (Fig. 3), sample 6), and (iv) an undoped sample, gated with gold for studying the electric field dependence (Fig. 2c and SI Fig. S1, sample 5). Samples 3, 4, 5, and 6 were prepared by the Minnesota and Zagreb groups from commercial crystals (MTI Corp.). Sample 1 was polished extensively after its deformation in order to reduce the surface roughness induced by the deformation. However, the stress appears to have destroyed the dislocation structure. The polishing appears to have missed a small region, and that is probably the reason

for the inhomogeneous surface profile noted in the Results section, and in SI Figs. S4 and S5.

### Micro-SQUID setup

The SQUID sensor consisting of a 1.5  $\mu\text{m}$  or 7  $\mu\text{m}$  diameter pick-up loop was used in experiments at Bar-Ilan or Connecticut, respectively. The pick-up loop detects the magnetic field. Additionally, the sensors have an integrated micro-field coil that applies an alternating local excitation field. By combining a low-pass filter and a lock-in technique, we simultaneously record both spontaneous and field-generated magnetism and reliably distinguish between the two. During the scanning process, the SQUID tip is 0.2–2  $\mu\text{m}$  above the sample surface or in contact with it. Scanning at different heights using a non-contact mode does not yield any magnetic response (see SI Fig. 6). To establish contact, we use piezoelectric elements to press a nonconducting silicon chip onto the sample surface. We record the change of capacitance resulting from the bending of a flexible cantilever during scanning, which corresponds to the force applied by the piezoelectric elements. The stress profile is triaxial, dome-shaped, centered around the contact point. In previous works, we estimated the force by cantilever deflection to be around 0.1–1  $\mu\text{N}$ <sup>33,57,58</sup>. However here we expect the profile to be more complicated than a simple dome, due to the two-dimensional deformations. In the low-stress regime, where we operate, we read the force exerted on the sample by the cantilever by a capacitor. The beam deflection after contact linearly changes the spacing between the capacitor plates.

### Scanning near-field optical microscopy measurements

We conducted nanoscale infrared imaging and spectroscopy of plastically deformed undoped STO crystals using a Park Systems NX-10 atomic force microscope (AFM) modified to function as a scattering-type near-field optical microscope (s-SNOM), using a home-built asymmetric Michelson interferometer with dual imaging and spectroscopy modalities. Mid-infrared light was sourced from a difference-frequency generation module pumped by the fiber feedback-stabilized optical parametric amplifier of an ultrafast laser system (MIR, Alpha-HP, and Primus units from Stuttgart Instruments), supplying 500 ps infrared pulses with 50  $\text{cm}^{-1}$  bandwidth at 40 MHz repetition rate. The laser frequency was tuned to an infrared frequency  $\omega \approx 750 \text{ cm}^{-1}$  ( $\approx 90 \text{ meV}$ )<sup>49</sup>, corresponding to the highest energy optical phonon. We focused this light to the sharp tip of a metallic microcantilevered AFM probe, which subsequently scattered in a manner determined by the complex permittivity of the sample volume proximate to the tip, whose apex radius determines the optical spatial resolution. A cryogenically cooled mercury cadmium telluride photoconductive detector (Judson Teledyne) recorded scattered infrared light which we demodulated (HF2LI from Zurich Instruments) at the third harmonic of the AFM probe oscillation (at 75 KHz, using an FM-PtSi probe from NanoSensors) for background suppression. By placing the s-SNOM and sample at one arm of the interferometer we could simultaneously extract the amplitude and phase of scattered light<sup>59</sup>. We conducted the nano-infrared imaging (Fig. 3a, b) and spectroscopy measurements (see SI) on the deformed STO sample via time-resolved pseudo-heterodyne imaging<sup>60</sup> and nanoscale Fourier transform infrared spectroscopy methods<sup>61</sup>, respectively. NanoFTIR spectra were synthesized by merging several distinct spectra acquired at incremental tunings of the characteristic energy of the MIR stage output (from 600 to 1000  $\text{cm}^{-1}$ ).

The interference pattern we recorded directly reports on the local strength of elastic strains near the tip. The visibility of these strains follows from the vibrational Grüneisen effect (see SI)<sup>50</sup>, in which the local optical phonon energy is shifted from its unstrained value in direct proportion to the local elastic strain. Earlier SNOM studies of polar semiconductors have shown this effect can directly modulate the optical phonon response in real-space<sup>62</sup>, as we observe here. By combining our dedicated nano-spectroscopy measurements of the optical

phonon in our STO sample with previously measured values for the Grüneison constant of this mode (see SI), a rudimentary analysis suggests strain variations, averaged over our resolution, on order of 0.1%. However, as is well known, dislocation-induced strain patterns are multipolar in nature, and furthermore the pattern from the wall is periodic (i.e. along the  $z$  axis in Fig. 4 (see SI, Fig. S9)). This implies that the averaged signal is reduced by a factor of  $(h/W)^\alpha (h/D)^{\alpha'}$ , where  $W \sim 10\text{nm}$ ,  $D \sim 50\text{nm}$  are respectively the width and penetration depth of quasi-electrostatic near-fields localized near the optical nano-probe, and  $\alpha, \alpha'$  are constants of order one that depend on the details of the beam profile and the surface boundary effects. Hence we may expect local strain variations are on order of 1–10%.

### Estimating the magnitude of the magnetic moments

Our experiment does not give us a quantitative measurement of the magnetic moments in the sample. However, it is possible to make an order-of-magnitude estimate. Our pickup loop resides at a height  $z_0 \sim 1\ \mu\text{m}$  above the sample surface, and its radius is also  $R \sim 1\ \mu\text{m} \sim z_0$ . In addition, the contact tip is situated several microns from the loop center, and has a submicron contact region. Thus, all relevant lengths are of the same order and for simplicity in what follows we take them all  $\sim z_0$ . We verified that this approximation is an *underestimation*.

We start with an estimate of the effective magnetization at the surface disregarding any microscopic considerations such as the dislocation walls. Since strain decays algebraically, we may assume that only magnetic moments within a distance on the order of microns from the tip are rotated out of the plane. We therefore assume a patch of  $\hat{z}$  polarized surface with a mean surface magnetization  $m_S$  and area  $\sim z_0^2$ . The standard expressions for the magnetic fields yield an average  $B \sim (\mu_0/4\pi)m_S/z_0$ , where  $m_S$  has units of Ampere (magnetization per area). This implies the average flux measured by the SQUID is

$$\Phi \sim \frac{\mu_0 m_S}{4\pi} \left( \frac{R^2}{z_0} \right) \sim \mu_0 m_S z_0. \quad (2)$$

Our mean measured flux at the highest stress is  $\Phi - 0.01\Phi_0$ , where  $\Phi_0$  is the flux quantum. Plugging these expressions back into Eq. (2) we find that  $m_S \sim \mu_B/a^2$ , with a coefficient of order one.

Let us now try to assume that the magnetization is supplied by the dislocation walls, and estimate the magnetization per dislocation. We can obtain a rough estimate of the dislocation density by assuming each dislocation wall removed one unit cell length from the sample, yielding an average inter-wall separation of  $d \sim a/\epsilon$ , where  $\epsilon \sim 0.01$  is the deformation of the sample. We assume that the surface magnetization calculated above is supplied by the infinite set of dislocations running parallel to the surface at increasing distances and that the strain rotates dislocations only up to a depth of order  $z_0$ . In that case, we may estimate  $m \sim m_S/z_0$ , where  $m$  is now the bulk magnetization (in Ampere/meter) from the dislocation distribution. A unit-cell of the dislocation wall has a width of  $d$ , depth of  $h$ , and height of  $a$ . Thus,

$$m \sim \frac{m_S}{z_0} \sim \frac{\mu_B}{adh} \left( \frac{h}{\epsilon z_0} \right) = 0.6 \frac{\mu_B}{adh} \quad (3)$$

so that we have approximately one Bohr-magneton per layer in each dislocation. We note our estimates are rather conservative since we assumed the tip fully polarizes the magnetic moments and ignored any possible spiral order.

### Theoretical modeling

As described in the main text, we describe our system via a Ginzburg-Landau free energy that couples magnetism, ferroelectricity, and

strain. Its form is

$$F = F_m + F_u + F_{me} + F_{ue} + F_{mu}, \quad (4)$$

where  $F_m$  denotes the magnetic free energy,  $F_u$  denotes the FE free energy, and  $F_{me}, F_{ue}$  denote the magneto- and ferro- elastic coupling.

**Magnetic order.** For the magnetic free energy terms we take,

$$F_m = \int dx dz \left[ \frac{1}{2} a_m |\mathbf{m}|^2 + \frac{1}{4} b_m \sum_i m_i^4 - \frac{1}{2} c_m \mathbf{m} \cdot \nabla^2 \mathbf{m} \right] \quad (5)$$

$$F_{me} = \frac{1}{2} \int dx dz \left( \lambda_1^{me} \epsilon_0 |\mathbf{m}|^2 + \lambda_2^{me} \left[ (2\epsilon_{xx} - \epsilon_{yy}) m_x^2 + (2\epsilon_{yy} - \epsilon_{xx}) m_y^2 - \lambda_3^{me} \epsilon_0 m_z^2 \right] \right), \quad (6)$$

where,  $i \in \{1, 2, 3\}$ ,  $\epsilon_0 = \epsilon_{xx} + \epsilon_{yy}$  is the compressive strain, and  $\lambda_j^{mu}$  denote respectively coupling to volume-changing, volume-preserving, and shear strain, which are the allowed terms in a cubic lattice (which we take for simplicity). The quadratic-linear coupling implies that  $|\mathbf{m}| \sim \sqrt{\epsilon}$  upon ordering. We do not know a-priori the values of the various couplings, however, our results do not strongly depend on the values, provided  $a_m \lesssim \lambda$ . In our numerics we take  $\lambda_3^{me} = 0$  for simplicity.

As discussed above, previous work has established that the dislocation Burgers vectors are positioned approximately equidistantly with a spacing of  $h \approx 14a_0$  in walls lying in the  $yz$  plane. We assume that the signal is dominated by dislocations parallel to the measurement  $xy$  plane, hence the Burgers vectors in our wall have following pattern (see Fig. 4),  $\mathbf{b}_n = b_0 [\hat{x} + (-1)^n \hat{z}]$ ;  $\forall n \in (-\infty, \infty)$ . Each dislocation  $\mathbf{b}_n$  creates a displacement  $\mathbf{w}_n$ , with

$$\mathbf{w}^n = (-1)^n \frac{1}{8\pi} \left[ \frac{\cos(2\phi) \mathbf{b}_n + (1 - (-1)^n \sin(2\phi)) \mathbf{b}_{n+1}}{(1 - \sigma)} + \frac{(1 - 2\sigma)}{(1 - \sigma)} \log(r^2) \mathbf{b}_{n+1} + 4 \tan^{-1} \left( \frac{\sin(\phi) + \cos(\phi)}{\cos(\phi) - \sin(\phi)} \right)^{(-1)^n} \right] \mathbf{b}_n, \quad (7)$$

where,  $r^2 = x^2 + z^2$ ,  $\phi = \tan^{-1}(z/x)$  and  $\sigma = 0.24$  is the Poisson ratio. The strain tensors are as usual  $\epsilon_{ij}(x, z) = (1/2) (\partial w_i / \partial r_j + \partial w_j / \partial r_i)$ , and the total strain field is obtained by summing up the infinite series for the wall. (We note that the physical wall is actually half-infinite only. However, this only gives rise to a boundary region of width  $\sim h$  which we neglect.) The resulting strain field for a consecutive pair of Burgers vectors oscillates along the  $z$ -direction, i.e. away from the measurement surface, with periodicity  $2h$ , and it decays exponentially away from the wall ( $\epsilon_{ij} \propto e^{-|x|/h}, e^{-2|x|/h}$  at large  $|x|$ ). We plug the fields back into the free energy, Eq. (5) and solve the resulting system numerically via a standard relaxation method. Starting from an initially weak spin-ordering this modified coefficient leads to the ferromagnetic/antiferromagnetic ‘puddle’-like structure. For  $c_m = 0$ , the different puddles are completely independent, and this degeneracy is only weakly lifted by the gradient term, due to a  $z$ -axis inversion symmetry (see Fig. 5). As discussed in the main text, for generic coefficients all  $m_i \neq 0$ .

**FE order.** The FE free energy has the same form as the magnetic one, see Eqs. (1) and (5). The coefficients  $a_u, \lambda_j^{ue}$  have been previously estimated from DFT<sup>16,51</sup>, which means that  $\mathbf{u}(x, z)$  can be computed explicitly, at least for  $c_u = 0$ . Taking  $c_u > 0$  does not qualitatively change the result. As discussed in the main text, since  $\nabla \cdot \mathbf{u} \approx 0$ , the FE order must be parallel to the dislocation lines, i.e.  $\mathbf{u} = u_y(x, z)\hat{y}$ , see Fig. 6.

**The magneto-polar coupling.** Next we consider the possible magneto-polar interactions. The simplest coupling is just fully-symmetric under all lattice transformations, namely,  $F_{mu} = \int dx dz \frac{1}{2} Q_{mu} |\mathbf{m}|^2 |\mathbf{u}|^2$ . Previous experiments in deformed STO found that the FE mode decreases (roughly linearly) with temperature



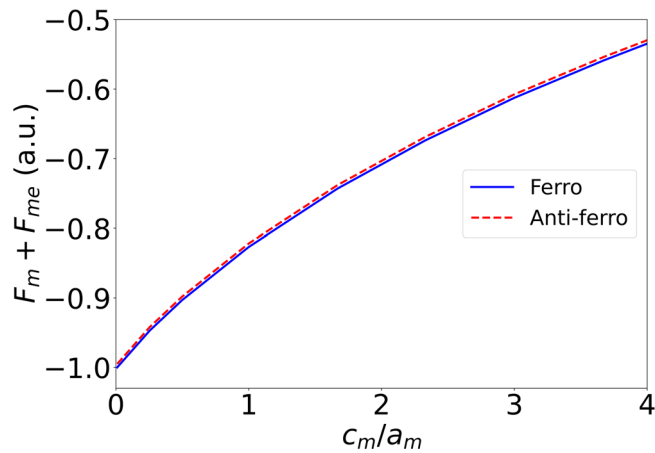


**Fig. 5** | Almost degeneracy of the free energy for ferromagnetic and anti-ferromagnetic puddle configurations.

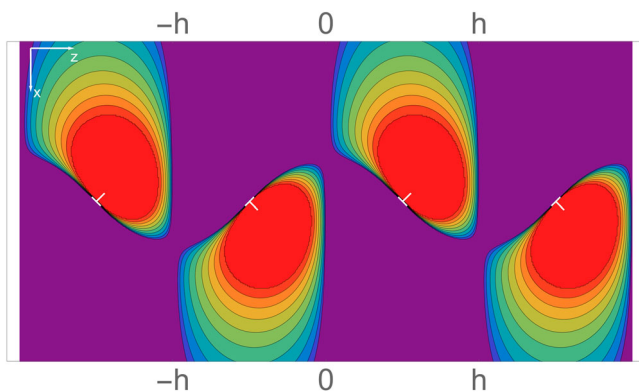


**Fig. 6** | The FE order along the dislocation walls. The intensity map corresponds to  $u_y$  (arbitrary units). For simplicity we set  $c_u = 0$ . At nonzero  $c_u$  the ordered regions will merge together and create long-range order.

up to some rather high  $T_{FE} > 100\text{K}$ . Thus, the temperature dependence  $\mathbf{m}(T)$  depicted in Fig. 2b is consistent with  $Q_{mu} > 0$ . Indeed, the coupling just renormalizes the magnetic  $a_m$ , namely,  $a_m \rightarrow a_m + Q_{mu}|\mathbf{u}|^2 \approx a_m + Q_{mu} \frac{A_0 + a_0(T_{FE} - T)}{b_u}$  where  $A_0$  is the average strain-induced correction to  $a_u = a_0(T_{FE} - T)$ . Crucially, we see that  $a_m$  decreases and therefore  $|\mathbf{m}|$  increases with increasing temperature. The second possible coupling is a magneto-polar-elastic coupling where  $\mathbf{u}$  appears linearly and inversion symmetry is restored by a gradient operator. To understand the impact of this coupling, we recall that a key difference between the magnetic and FE modes is, that the magnetic moments are localized forming ‘puddles’ along the dislocation lines, but the FE mode has long-range order. We therefore coarse-grain each dislocation wall into a series of “spins” running along  $z$  with magnitude  $m_n \sim (\lambda^{me} \epsilon)^{1/2} h^2$ , and similarly for the FE mode. This means we can treat each wall as a 1D chain, and for simplicity we assume the spins have constant magnitude  $m_0$ , and the FE order is constant in both magnitude and direction. In that case the lowest order coupling is just  $F_{mue} = \int dz Q_{mue} m_y(z) u_y \partial_z m_z(z)$ , with  $Q_{mue}$  being the coupling constant. The gradient term induces a helical configuration for the spins along the out-of-plane  $z$ -direction. To see this it is convenient to study the system in the single-mode approximation  $m_x = \text{const}$ ,  $m_y = m_0 \cos(qz)$ ,  $m_z = m_0 \sin(qz)$ . A solution exists with a nonzero  $q = -Q_{mue} u_y / (2c_m)$ , which is a minimum of the free energy for  $u_y^2 > N_{mue} b_m c_m m_0^2 / Q_{mue}^2$ , where  $N_{mue} = O(1)$  is some numerical coefficient. Note that when  $c_m$  goes to zero the spiral is always preferred.

## Data availability

All the data used in this work are available upon request from the corresponding authors.

## Code availability

All the code used in this work is available upon request from the corresponding authors.

## References

- Giustino, F. et al. The 2021 quantum materials roadmap. *J. Phys. Mater.* **3**, 042006 (2021).
- Hwang, H. Y. et al. Emergent phenomena at oxide interfaces. *Nat. Mater.* **11**, 103–113 (2012).
- Zunger, A. & Malyi, O. I. Understanding doping of quantum materials. *Chem. Rev.* **121**, 3031–3060 (2021).
- Maiti, A. Bandgap engineering with strain. *Nat. Mater.* **2**, 440–442 (2003).
- Schlom, D. G. et al. Strain tuning of ferroelectric thin films. *Annu. Rev. Mater. Res.* **37**, 589–626 (2007).
- MacManus-Driscoll, J. L. et al. Strain control and spontaneous phase ordering in vertical nanocomposite heteroepitaxial thin films. *Nat. Mater.* **7**, 314–320 (2008).
- Tan, S. et al. Interface-induced superconductivity and strain-dependent spin density waves in FeSe/SrTiO<sub>3</sub> thin films. *Nat. Mater.* **12**, 634–640 (2013).
- Ahadi, K. et al. Enhancing superconductivity in SrTiO<sub>3</sub> films with strain. *Sci. Adv.* **5**, 4 (2019).
- Herrera, C. et al. Strain-engineered interaction of quantum polar and superconducting phases. *Phys. Rev. Mater.* **3**, 124801 (2019).
- Nova, T. F., Disa, A. S., Fechner, M. & Cavalleri, A. Metastable ferroelectricity in optically strained SrTiO<sub>3</sub>. *Science* **364**, 1075–1079 (2019).
- Liu, D. et al. Strain analysis and engineering in halide perovskite photovoltaics. *Nat. Mater.* **20**, 1337–1346 (2021).
- Hansen, N. & Barlow, C. 17 - plastic deformation of metals and alloys. In *Physical Metallurgy (Fifth Edition)* (eds Laughlin, D. E. & Hono, K.) 1681–1764, (Elsevier, Oxford, 2014).
- Kumar, S. & Povoden-Karadeniz, E. Plastic deformation behavior in steels during metal forming processes: a review. *Mater. Flow Anal.* (2021).
- Sypek, J. T. et al. Superelasticity and cryogenic linear shape memory effects of CaFe<sub>2</sub>As<sub>2</sub>. *Nat. Commun.* **8**, 1083 (2017).
- Xiao, S. et al. Pseudoelasticity of SrNi<sub>2</sub>P<sub>2</sub> micropillar via double lattice collapse and expansion. *Nano Lett.* **21**, 7913–7920 (2021).
- Hameed, S. et al. Enhanced superconductivity and ferroelectric quantum criticality in plastically deformed strontium titanate. *Nat. Mater.* **21**, 54–61 (2022).
- Li, M. et al. Tailoring superconductivity with quantum dislocations. *Nano Lett.* **17**, 4604–4610 (2017).
- Li, M. Quantized dislocations. *J. Phys. Condens. Matter* **31**, 083001 (2019).
- Scheerer, G. et al. Ferroelectricity, superconductivity, and SrTiO<sub>3</sub> – passions of K.A. Müller. *Condens. Matter* **5**, 4 (2020).
- Zubko, P., Catalan, G., Buckley, A., Welche, P. R. L. & Scott, J. F. Strain-gradient-induced polarization in SrTiO<sub>3</sub> single crystals. *Phys. Rev. Lett.* **99**, 167601 (2007).
- Song, Q. et al. Evidence of cooperative effect on the enhanced superconducting transition temperature at the FeSe/SrTiO<sub>3</sub> interface. *Nat. Commun.* **10**, 758 (2019).
- Xu, R. et al. Strain-induced room-temperature ferroelectricity in SrTiO<sub>3</sub> membranes. *Nat. Commun.* **11**, 3141 (2020).
- Enderlein, C. et al. Superconductivity mediated by polar modes in ferroelectric metals. *Nat. Commun.* **11**, 4852 (2020).
- Gastiasoro, M. N., Ruhman, J. & Fernandes, R. M. Superconductivity in dilute SrTiO<sub>3</sub>: a review. *Ann. Phys.* **417**, 168107 (2020).



25. Haeni, J. H. et al. Room-temperature ferroelectricity in strained SrTiO<sub>3</sub>. *Nature* **430**, 758–761 (2004).
26. Pai, Y.-Y., Tylan-Tyler, A., Irvin, P. & Levy, J. Physics of SrTiO<sub>3</sub>-based heterostructures and nanostructures: a review. *Rep. Prog. Phys.* **81**, 036503 (2018).
27. Li, L., Richter, C., Mannhart, J. & Ashoori, R. C. Coexistence of magnetic order and two-dimensional superconductivity at LaAlO<sub>3</sub>/SrTiO<sub>3</sub> interfaces. *Nat. Phys.* **7**, 762–766 (2011).
28. Bert, J. A. et al. Direct imaging of the coexistence of ferromagnetism and superconductivity at the LaAlO<sub>3</sub>/SrTiO<sub>3</sub> interface. *Nat. Phys.* **7**, 767–771 (2011).
29. Ariando. Electronic phase separation at the LaAlO<sub>3</sub>/SrTiO<sub>3</sub> interface. *Nat. Commun.* **2**, 188 (2011).
30. Kalisky, B. et al. Critical thickness for ferromagnetism in LaAlO<sub>3</sub>/SrTiO<sub>3</sub> heterostructures. *Nat. Commun.* **3**, 922 (2012).
31. Lee, J.-S. et al. Titanium dxy ferromagnetism at the LaAlO<sub>3</sub>/SrTiO<sub>3</sub> interface. *Nat. Mater.* **12**, 703–706 (2013).
32. Yang, M. et al. Direct observation of room-temperature stable magnetism in LaAlO<sub>3</sub>/SrTiO<sub>3</sub> heterostructures. *ACS Appl. Mater. Interfaces* **10**, 9774–9781 (2018).
33. Christensen, D. V. et al. Strain-tunable magnetism at oxide domain walls. *Nat. Phys.* **15**, 269–274 (2019).
34. Basini, M. et al. Terahertz electric-field-driven dynamical multiferroicity in SrTiO<sub>3</sub>. *Nature* **628**, 534–539 (2024).
35. Coey, J. M. D., Venkatesan, M. & Stamenov, P. Surface magnetism of strontium titanate. *J. Phys. Condens. Matter* **28**, 485001 (2016).
36. Bi, F. et al. Room-temperature electronically-controlled ferromagnetism at the LaAlO<sub>3</sub>/SrTiO<sub>3</sub> interface. *Nat. Commun.* **5**, 5019 (2014).
37. Park, D.-S. et al. The emergence of magnetic ordering at complex oxide interfaces tuned by defects. *Nat. Commun.* **11**, 3650 (2020).
38. Shein, I. & Ivanovskii, A. First principle prediction of vacancy-induced magnetism in non-magnetic perovskite SrTiO<sub>3</sub>. *Phys. Lett. A* **371**, 155–159 (2007).
39. Banerjee, S., Erten, O. & Randeria, M. Ferromagnetic exchange, spin-orbit coupling and spiral magnetism at the LaAlO<sub>3</sub>/SrTiO<sub>3</sub> interface. *Nat. Phys.* **9**, 626–630 (2013).
40. Chikina, A. et al. Orbital ordering of the mobile and localized electrons at oxygen-deficient LaAlO<sub>3</sub>/SrTiO<sub>3</sub> interfaces. *ACS Nano* **12**, 7927–7935 (2018).
41. Rata, A. D. et al. Defect-induced magnetism in homoepitaxial SrTiO<sub>3</sub>. *APL Mater.* **10**, 091108 (2022).
42. Nakamura, Y. & Yanase, Y. Multi-orbital superconductivity in SrTiO<sub>3</sub>/LaAlO<sub>3</sub> interface and SrTiO<sub>3</sub> surface. *J. Phys. Soc. Jpn.* **82**, 083705 (2013).
43. Salmani-Rezaie, S. et al. Superconductivity in magnetically doped SrTiO<sub>3</sub>. *Appl. Phys. Lett.* **118**, 202602 (2021).
44. Gumbsch, P., Taeri-Baghadrani, S., Brunner, D., Sigle, W. & Rühle, M. Plasticity and an inverse brittle-to-ductile transition in strontium titanate. *Phys. Rev. Lett.* **87**, 085505 (2001).
45. Chen, H., Yi, D., Xu, B., Ma, J. & Nan, C. Spontaneous symmetry breaking of dislocation core in SrTiO<sub>3</sub>. *Mater. Today Phys.* **20**, 100453 (2021).
46. Rowley, S. E. et al. Ferroelectric quantum criticality. *Nat. Phys.* **10**, 367–372 (2014).
47. Chen, X. et al. Modern scattering-type scanning near-field optical microscopy for advanced material research. *Adv. Mater.* **31**, 1804774 (2019).
48. Lewin, M. et al. Nanospectroscopy of infrared phonon resonance enables local quantification of electronic properties in doped SrTiO<sub>3</sub> ceramics. *Adv. Funct. Mater.* **28**, 1802834 (2018).
49. Varshney, S. et al. Hybrid molecular beam epitaxy for single-crystalline oxide membranes with binary oxide sacrificial layers. *ACS Nano* **18**, 6348–6358 (2024).
50. Guennou, M., Bouvier, P., Kreisel, J. & Machon, D. Pressure-temperature phase diagram of SrTiO<sub>3</sub> up to 53 gpa. *Phys. Rev. B Condens. Matter Mater. Phys.* **81**, 054115 (2010).
51. Dunnett, K., Narayan, A., Spaldin, N. A. & Balatsky, A. V. Strain and ferroelectric soft-mode induced superconductivity in strontium titanate. *Phys. Rev. B* **97**, 144506 (2018).
52. Franklin, J. et al. Giant grüneisen parameter in a superconducting quantum paraelectric. *Phys. Rev. B* **103**, 214511 (2021).
53. Gao, P. et al. Atomic-scale measurement of flexoelectric polarization at SrTiO<sub>3</sub> dislocations. *Phys. Rev. Lett.* **120**, 267601 (2018).
54. Hameed, S. et al. Nature of the ferromagnetic-antiferromagnetic transition in Y<sub>1-x</sub>La<sub>x</sub>TiO<sub>3</sub>. *Phys. Rev. B* **104**, 024410 (2021).
55. Juraschek, D. M., Fechner, M., Balatsky, A. V. & Spaldin, N. A. Dynamical multiferroicity. *Phys. Rev. Mater.* **1**, 014401 (2017).
56. Dunnett, K., Zhu, J.-X., Spaldin, N. A., Juričić, V. & Balatsky, A. V. Dynamic multiferroicity of a ferroelectric quantum critical point. *Phys. Rev. Lett.* **122**, 057208 (2019).
57. Kremen, A. et al. Mechanical control of individual superconducting vortices. *Nano Lett.* **16**, 1626–1630 (2016).
58. Kalisky, B. et al. Scanning probe manipulation of magnetism at the LaAlO<sub>3</sub>/SrTiO<sub>3</sub> heterointerface. *Nano Lett.* **12**, 4055–4059 (2012).
59. Ocelic, N., Huber, A. & Hillenbrand, R. Pseudoheterodyne detection for background-free near-field spectroscopy. *Appl. Phys. Lett.* **89**, 10 (2006).
60. Sternbach, A. J. et al. Artifact free time resolved near-field spectroscopy. *Opt. Express* **25**, 28589–28611 (2017).
61. Huth, F. et al. Nano-ftir absorption spectroscopy of molecular fingerprints at 20 nm spatial resolution. *Nano Lett.* **12**, 3973–3978 (2012).
62. Huber, A., Ziegler, A., Köck, T. & Hillenbrand, R. Infrared nanoscopy of strained semiconductors. *Nat. Nanotechnol.* **4**, 153–157 (2009).

## Acknowledgements

We thank N. Bachar, B. Davidovitch, J. Ruhman, P. Volkov, R. M. Fernandes, D. M. Juraschek and A. Balatsky for interesting discussions. We thank I. Khayr for sample preparation at the University of Minnesota. We thank A. V. Bjørlig for performing measurements on the deformed Nb doped sample 1, and J. Bedard and J. Franklin for performing measurements on Nb doped sample 2. The computational resources for this work were provided by the Ariel HPC Center at Ariel University. X.W., N.R., S.R. and B.K. were supported by the European Research Council Grant No. ERC-2019- OG-866236, the Israeli Science Foundation, grant No. ISF-228/22, COST Action CA21144, and the Pazy Research Foundation grant no. 107-2018. A. Kundu and A. Klein acknowledge funding from the Israel Science Foundation (ISF) and the Israeli Directorate for Defense Research and Development (DDR&D) under grant No. 3467/21. The work at University of Minnesota was funded by the Department of Energy through the University of Minnesota Center for Quantum Materials, under Grant No. DE-SC0016371. The work at the University of Zagreb was supported by the Croatian Science Foundation under grant No. UIP-2020-02-9494. The work at the University of Connecticut was supported by the National Science Foundation award No. 2233149.

## Author contributions

X.W., B.X., N.R., S.R., and B.K. performed scanning SQUID measurements and analyzed the data. B.X., L.R., S.H., and D.P. prepared deformed samples and characterized them. A.M. conceived the optical nano-imaging and -spectroscopy experiments, and L.T. performed them and analyzed nano-spectroscopy data. A. Kundu and A. Klein produced the theoretical model, and conducted the numerical simulations. M.G., I.S., A.M., D.P., B.K., and A. Klein conceived of the project and supervised it. All authors discussed and contributed to the final version of the manuscript.

## Competing interests

The authors declare no competing interests.

## Additional information

**Supplementary information** The online version contains supplementary material available at <https://doi.org/10.1038/s41467-024-51615-z>.

**Correspondence** and requests for materials should be addressed to Beena Kalisky or Avraham Klein.

**Peer review information** *Nature Communications* thanks Jianxin Lin, Jirong Sun and the other anonymous reviewer(s) for their contribution to the peer review of this work. A peer review file is available.

**Reprints and permissions information** is available at <http://www.nature.com/reprints>

**Publisher's note** Springer Nature remains neutral with regard to jurisdictional claims in published maps and institutional affiliations.

**Open Access** This article is licensed under a Creative Commons Attribution-NonCommercial-NoDerivatives 4.0 International License, which permits any non-commercial use, sharing, distribution and reproduction in any medium or format, as long as you give appropriate credit to the original author(s) and the source, provide a link to the Creative Commons licence, and indicate if you modified the licensed material. You do not have permission under this licence to share adapted material derived from this article or parts of it. The images or other third party material in this article are included in the article's Creative Commons licence, unless indicated otherwise in a credit line to the material. If material is not included in the article's Creative Commons licence and your intended use is not permitted by statutory regulation or exceeds the permitted use, you will need to obtain permission directly from the copyright holder. To view a copy of this licence, visit <http://creativecommons.org/licenses/by-nc-nd/4.0/>.

© The Author(s) 2024